Journal of Alloys and Compounds 989 (2024) 174321

Contents lists available at ScienceDirect

Journal of Alloys and Compounds

journal homepage: www.elsevier.com/locate/jalcom

Tuning the metal-insulator transition temperature by the controlled generation of oxygen vacancies on $La_{0.7}Ca_{0.3}MnO_{3-x}$ epitaxial thin films

E. Salas-Colera [a,b,c,*], A. Muñoz-Noval [d,e], E. Sebastiani-Tofano [a,b], G.R. Castro [a,b], J. Rubio-Zuazo [a,b]

[a] Spanish CRG BM25 Beamline SpLine at the ESRF, 71 avenue des Martyrs, Grenoble 38000, France
[b] Instituto de Ciencia de Materiales de Madrid-ICMM/CSIC, Sor Juana Inés de la Cruz 3, Cantoblanco, Madrid 28049, Spain
[c] Universidad Carlos III de Madrid, Departamento de Física, Av. de la Universidad 30, Leganés, Madrid 28911, Spain
[d] Universidad Complutense de Madrid, Departamento de Física de Materiales, Av. de la Complutense s/n, Madrid 28040, Spain
[e] Instituto Madrileño de Estudios Avanzados en Nanociencia - IMDEA Nanociencia, c) Faraday 9, Cantoblanco, Madrid 28049, Spain

ARTICLE INFO

Keywords:
Oxygen vacancies
Mixed valence manganites
Electronic properties
Metal-insulator transition
Polarized EXAFS

ABSTRACT

This report presents a study on the effect of the controlled generation of oxygen vacancies on the electronic transport properties of $La_{0.7}Ca_{0.3}MnO_{3-x}$ epitaxial thin films. Oxygen defects cause significant changes in the crystalline structure of mixed-valence manganites and lower the Mn valence, resulting in a shift of the metal-insulator transition to lower temperatures due to modifications in the angles and lengths of Mn-O bonds. Experiments using Polarized Extended X-Ray Absorption Fine Structure Spectroscopy have provided strong evidence that oxygen vacancies are mainly formed in the basal plane of the MnO_6 octahedra. The accurate control of oxygen vacancies generation opens possibilities for managing and enhancing the magneto-electronic properties of epitaxial manganite thin films with potential in industrial applications.

1. Introduction

Complex oxide compounds exhibit notable properties such as superconductivity, colossal magnetoresistance, ferroelectricity, and multiferroicity. These properties arise from the intricate interplay between charge, spin, chemical composition and lattice features. The perovskite material $La_{0.7}Ca_{0.3}MnO_3$ (LCMO) shows a ferromagnetic-paramagnetic phase transition simultaneous to a metal-insulator transition and colossal magnetoresistance [1] behavior near room temperature.

The structural [2] and morphological [3] characteristics of the LCMO are crucial in defining the macroscopic transport and magnetic properties exhibited by this material. According to the double-exchange model, the itinerant charge carriers provide the mechanism for the ferromagnetic interaction between Mn^{3+} and Mn^{4+} ions [4]. The coupling between holes and electrons is highly dependent on the structural properties of MnO_6 octahedra, such as the angle of Mn-O-Mn and the distance of the Mn-O bond [5].

A method for modifying structural properties is through the controlled growth of epitaxial thin films. The epitaxial strain induces lattice distortions, allowing for a controlled tuning of the macroscopic response through epitaxial strain engineering. In this sense, thin films have potential applications in magneto-electronic devices [6,7]. However, reducing the thickness substantially modifies the magnetic and electronic properties [8]. While ultra-thin films have yielded extremely large magnetoresistance values [9–11], their transport properties are generally strongly degraded. Previous studies have suggested that the generation of oxygen defects is the main cause for the increase in resistivity and the decrease in the metal-to-insulator transition temperature. Oxygen defects are generated to relieve the epitaxial strain energy accumulated by the lattice and have a direct influence on the electron hopping between Mn^{3+} and Mn^{4+} ions, resulting in a modification of the magneto-electronic properties displayed [4].

In this sense, based on the direct relation between oxygen vacancies and transport response, the controlled generation of oxygen vacancies in this material can be used as a mechanism to tune the magneto-electronic properties [12–14]. However, a complete understanding of the influence of oxygen vacancies on the structural and transport properties is required.

Some articles [15–20] report on theoretical studies that used density functional theory to investigate the formation and stability of oxygen

* Corresponding author at: Universidad Carlos III de Madrid, Departamento de Física, Av. de la Universidad 30, Leganés, Madrid 28911, Spain.
E-mail address: esalas@fis.uc3m.es (E. Salas-Colera).

https://doi.org/10.1016/j.jallcom.2024.174321
Received 27 December 2023; Received in revised form 22 March 2024; Accepted 27 March 2024
Available online 28 March 2024

vacancies in cubic ABO_3 type perovskites. The stability of vacancies is found to be correlated with the ionic radius of elements and the bulk formation energy. The latter can be decomposed into the ionization energy and lattice energy. However, the formation of oxygen vacancies in perovskite system is dependent on the atomic concentration of A and B elements, which can modify the formation energy of these oxygen vacancies.

In a previous experiment [12], oxygen vacancies were generated in epitaxial ultra-thin LCMO films in a controlled way. A correlation between the electronic, transport and structural properties of the films was observed as a function of the oxygen deficiencies. The results obtained suggest that oxygen vacancies are accommodated in the basal plane of the octahedral MnO_6 structure of the perovskite compound. However, direct evidence of the accumulation of vacancies in the basal plane had not been provided yet. To understand the mechanisms of electron transport, it is necessary to determine the location of oxygen vacancies within the unit lattice and evaluate the structural deformations around the oxygen defect. The aim of this study is to clarify the role of oxygen vacancies in lattice deformation and transport response using the polarized EXAFS (P-EXAFS) technique in epitaxially grown samples. EXAFS technique carried out in the Mn K-edge is highly sensitive to the structural properties of the first coordination shell in the LCMO compound surrounding the Mn ion. P-EXAFS takes advantages of the polarization of X-Rays from a synchrotron source to differentiate between the contributions to the EXAFS signal from the basal oxygen (in-plane) and apical oxygen (out-of-plane) in the octahedral MnO_6 structure.

2. Experimental

High quality epitaxial $La_{0.7}Ca_{0.3}MnO_3$ thin film (20 nm thick) was grown on a high quality $SrTiO_3$ (001) substrate using Pulsed Laser Deposition (PLD) method [12]. The PLD system uses a Nd:YAG 355 nm wavelength laser, which was operated at 10 Hz and 1 J/cm^2 irradiance power during the deposition process. A stoichiometric polycrystalline $La_{0.7}Ca_{0.3}MnO_3$ target was used. The thin film was deposited in an oxygen atmosphere of 2 mbars, keeping the substrate at room temperature. After the growth, the sample was annealed at 1000 K in 1 bar of flowing oxygen for 40 min. High crystallinity and flat interfaces were revealed by XRD and XRR [12].

Oxygen vacancies were generated in a controlled way by heating the sample under ultra-high vacuum conditions. The base pressure was $1.5\bullet10^{-6}$ mbar, the temperature was set at 673 K and the accumulated heating time was 10, 20, 50, 100 and 150 minutes. P-EXAFS characterization was subsequently carried out once the sample was cooled down to room temperature. Following each annealing treatment, temperature dependent transport measurements in the film plane were performed using the four probe method and an Oxford CV-F Optistat liquid helium (LHe) cryostat. Five different heating treatments were performed in order to reach different levels of oxygen vacancies in the sample.

P-EXAFS measurements were carried out at the Spanish CRG BM25 SpLine beamline [21] of The European Synchrotron ESRF. The EXAFS spectra at the Mn K-edge (6539 eV) were measured in the fluorescence yield mode using a Sirius multi-element solid state detector provided by e2v. The detector is equipped with 13 nitrogen liquid cooled Si(Li) crystal sensor detection elements. The analysis of the EXAFS data was performed using the Demeter software package [22].

X-rays from synchrotron radiation sources are highly polarized in the orbit plane. The shape of EXAFS spectra, thus the amplitude of radial structure functions, strongly depends on the geometry of the experiment. The amplitude of the EXAFS signal is determined by the angle between the electric-field vector of the X-ray beam and the vector linking the absorber and backscattering atoms [23]. The angular dependence of the EXAFS signal can be expressed as

$$\chi(k,\theta) = \sum_j \sum_{i=1}^{N_j} 3\cos^2(\theta_i^j)\chi_{iso}^j \quad (1)$$

where j is the number of neighboring atoms, i runs over all the N_j atoms and $\theta_i{}^j$ is the angle between the electric field vector and the vector R_{ij} of each atom in respect to the absorber.

If the sample is perfectly crystalline and symmetrically oriented around the (001) axis of manganite, which is perpendicular to the substrate surface, this equation can be simplified to obtain a direct relationship between the number of neighbors and the geometrical configuration of the backscattering atom in the sample

$$N_{eff} = 3N_{crys}\left[\cos^2\phi\sin^2\alpha + \frac{\cos^2\alpha\sin^2\phi}{2}\right] \quad (2)$$

where N_{eff} is the effective number of neighbors measured by the P-EXAFS signal for specific geometric experimental conditions, N_{crys} is the crystallographic number of neighbors, α is the angle between the electric field and the (001) axis, and ϕ is the angle between R_{ij} and the (001) axis. Eq. (2) clearly shows that the amplitude of the EXAFS signal is geometrically dependent.

Bulk perovskite LCMO has an octahedral structure surrounding the absorbing Mn atom. It is composed of four oxygen atoms on the basal plane and two apical oxygen atoms. The octahedra is slightly distorted and tilted with respect to the (001) axis. This distortion and tilting are determined by the tolerance factor t. Typical values for bulk LCMO are t = 0.917 which results in a Mn-O-Mn bond angle along the z-axis that is close to the ideal 180° [24]. In that situation, if the X-ray beam is applied at normal incidence ($\alpha = 0°$) regarding to the normal vector of the substrate surface, the contribution to the EXAFS signal from the apical oxygens ($\phi = 0°$) can be neglected and the EXAFS signal comes exclusively from the basal oxygens ($\phi = 90° \rightarrow N_{eff} = 3/2\, N_{basal}$). On the other hand, in grazing incidence ($\alpha = 90°$), the EXAFS signal corresponds to the contribution from apical atoms ($\phi = 0° \rightarrow N_{eff} = 3N_{apical}$) as the signal from the basal oxygen vanishes.

Polarized measurements were carried out in the epitaxial samples with the X-Ray polarization vector oriented either parallel or perpendicular to the normal vector of the sample surface. In the experimental set-up, alpha angle was fixed to $\alpha = 75°$, in grazing incidence, and $\alpha = 15°$ in normal incidence in order to accommodate the UHV chamber and the fluorescence detector. Therefore, the EXAFS signal will be dominated by one type of oxygen atoms. However, due to the non-perfect grazing and normal incidences, a residual contribution of the other type of oxygen atoms will be present. The contribution of the residual type of oxygen for each different configuration has been calculated using Eq. (2), taking into account the geometrical configuration of P-EXAFS experiment. The residual contribution is approximately 7% of the measured EXAFS signal.

EXAFS analysis was carried out for each annealing stage in both grazing and normal incidence. Initially, data reduction (removing pre-edge, post–edge, background subtraction and normalization) was performed using the ATHENA software. EXAFS analysis was performed using the ARTEMIS software. K-range was selected between 3.05 and 9.80 Å^{-1}. Fourier Transform was applied in that range using a Hanning window.

Fitting was calculated in the R-space, in a range from 1.15 to 4.35 Å, covering both first and second shells. This range of fitting includes more than 13 independent points according to the Nyquist criterion. The $LaMnO_3$ sample CIF file (taken from reference [25]) was used to generate scattering paths. All single scattering paths within that range were considered. Also, multiple scattering paths with more than 10% probability were included. The first shell was fitted using one single scattering path for all the oxygen atoms, taking into account the effective coordination number of neighbors to define the degeneracy of the path. The second shell was fitted using four single scattering paths for La

atoms, with degeneracy of 2 for each one and starting at distances of 3.26, 3.33, 3.38 and 3.44 Å. In addition, one single scattering path for Mn atoms, centered at 3.86 Å with a degeneracy of 6 was used. Finally, several multiples scattering were include in the fit: O-O double scattering (3.35 Å), O-Mn obtuse triangle (3.90 Å), O-O non forward linear (3.93 Å) and O-Mn-O forward triangle (3.93 Å).

The first step was to fit the as-grown sample to calculate the energy shift (E_0) and the passive electron reduction factor (S_0^2) parameters for each element (O, La and Mn). The energy shift E_0 calibrates the energy grid of the measured spectrum [26] with the theoretical calculated spectrum. The passive electron reduction factor [27] is an experimental parameter that evaluates the quantity of electron excitations without contribution to the fine structure. This calculated value of S_0^2 parameter was linked to the effective coordination number of neighbors in the absence of oxygen vacancies, as both parameters are fully correlated in the EXAFS equation [28]. The effective coordination number of neighbors for each annealing stage was then calculated by fitting the S_0^2 parameter. In addition to the S_0^2 parameter, the distance between neighbors (r) and the mean square displacement (σ^2) parameters were also fitted for oxygen atoms of the first atomic shell. The fitting parameters were selected as a function of the atomic element that generates the scattering path. For each EXAFS corresponding to a different annealing stage, the fitting parameters for each atomic element were the same. Finally, the contribution of the second shell was additionally fitted to refine the results. Regarding to the second shell scattering paths, the distance between neighbors (r) and the mean square displacement (σ^2) parameters were also fitted for both La and Mn scattering paths. Multiple scattering paths were defined as a combination of parameters used for single scattering paths; no additional parameters were used. This gives seven parameters to be fitted for each annealing state.

3. Results and discussion

Temperature dependent transport measurements were carried out for each stage of annealing treatment. The dependence of resistance as a function of temperature is shown in Fig. 1. It can be observed that the metal-to-insulator transition (MIT) temperature is obtained at 270 K for the as-grown sample. This value corresponds to the temperature reported for bulk LCMO. As the annealing time is increased, i.e. the amount of oxygen vacancies is increased, the MIT temperature shifts to lower temperatures, similarly to the study reported by Rubio-Zuazo et al. [12]. The MIT temperature decreases to 225 K, 194 K, 150 K, 119 K and 75 K for annealing at 673 K under UHV for 10, 20, 50, 100 and 150 minutes, respectively.

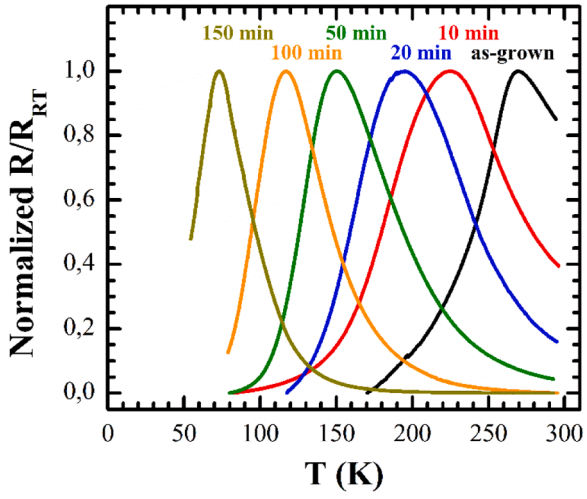

Fig. 1. Temperature dependent resistance curves for different annealing conditions. For better comparison, the resistance curves have been divided by the resistance at room temperature and normalized to one.

Fig. 2(a), (b), (c) and (d) show the comparison between the experimental spectra and the best fit of the modulus of Fourier Transform of $k^2\chi(k)$ EXAFS spectra for the as-grown and the 150 minutes annealed samples at 673 K under UHV conditions in both polarization geometries. The inset of each figure presents the real part of back Fourier Transform $q(R)$ to show the quality of the fitting.

P-EXAFS experiment was carried out to distinguish the contribution between of basal and apical oxygens in the EXAFS signal. Standard EXAFS experiments are not effective due to the close interatomic distance between the two types of oxygen atoms. The main fitting values obtained from the P-EXAFS analysis are shown in Fig. 3. The percentages of vacancies measured in each experimental configuration are plotted as a function of the annealing time in Fig. 3(a). Regarding to the experimental geometrical configuration, under normal incidence, the whole number of vacancies measured were produced in the basal oxygens. Conversely, under grazing incidence, the whole number of vacancies measured were produced in apical oxygens atoms. The percentages of vacancies were calculated by fitting the S_0^2 parameter for each annealing state and calculating the direct relation with the initial S_0^2 parameter obtained for the as-grown sample, which has a known value of oxygen atoms. The results show that the number of apical oxygen atoms remains constant for all annealing stages, as only a small number of vacancies between 1% and 2% were observed. On the contrary, the basal oxygen atoms are more sensitive to the sample annealing, showing a proportional increase in the number of vacancies with the annealing time. The number of oxygen vacancies produced at the basal plane reached 6.5% after an annealing time of 150 minutes.

Fig. 3(b) shows the evolution of the first neighbors distance with respect to the Mn absorbing atom as a function of the annealing time at a temperature of 673 K under UHV conditions. The distance of the basal oxygen increases with the annealing time, whereas the distance of the apical oxygen remains constant. The increase in bond length in the basal plane could be related to the lattice deformation mechanism in order to accommodate the presence of oxygen defects and the corresponding increase in Mn ionic radius due to the corresponding Mn valence reduction.

From Fig. 3(a) the total amount of oxygen vacancies generated can be calculated and correlated with the MIT temperature shift and the annealing time, as shown in Fig. 4. A clear exponential dependence of the total percentage of oxygen vacancies generated (exponential increase) and MIT temperature (exponential decrease) as a function of the annealing time is observed (Fig. 4(a)). This behavior suggests that low levels of oxygen vacancies can be easily generated with short annealing times at moderate temperatures. However, large annealing time is required to generate a significant number of oxygen defects. This is related to the lattice capabilities of assuming the oxygen defects through lattice deformation. As shown in Fig. 3(b), an exponential dependency of the apical oxygen bond length with the annealing time is also observed. For short annealing time, which corresponds to few oxygen defects, the bond length increases abruptly, however it increases slowly for larger annealing times. This fact suggests the initial oxygen defects are accommodated by lattice deformation, while a different mechanism occurs for a large amount of oxygen defects. Fig. 4(b) shows the MIT temperature dependency with the total amount of oxygen vacancies. A linear dependency is observed similar to that found in Ref. [12].

4. Conclusions

Polarized EXAFS has been successfully used to distinguish the contributions to the EXAFS signal from basal and apical oxygens in the octahedral MnO_6 structure during the generation of oxygen vacancies in $La_{0.3}Ca_{0.7}MnO_{3-x}$ epitaxial thin films. Oxygen vacancies have been produced by annealing treatments at a moderate temperature of 675 K under an ultra-high vacuum environment. It has been demonstrated that the oxygen effective coordination number decreases at the basal plane

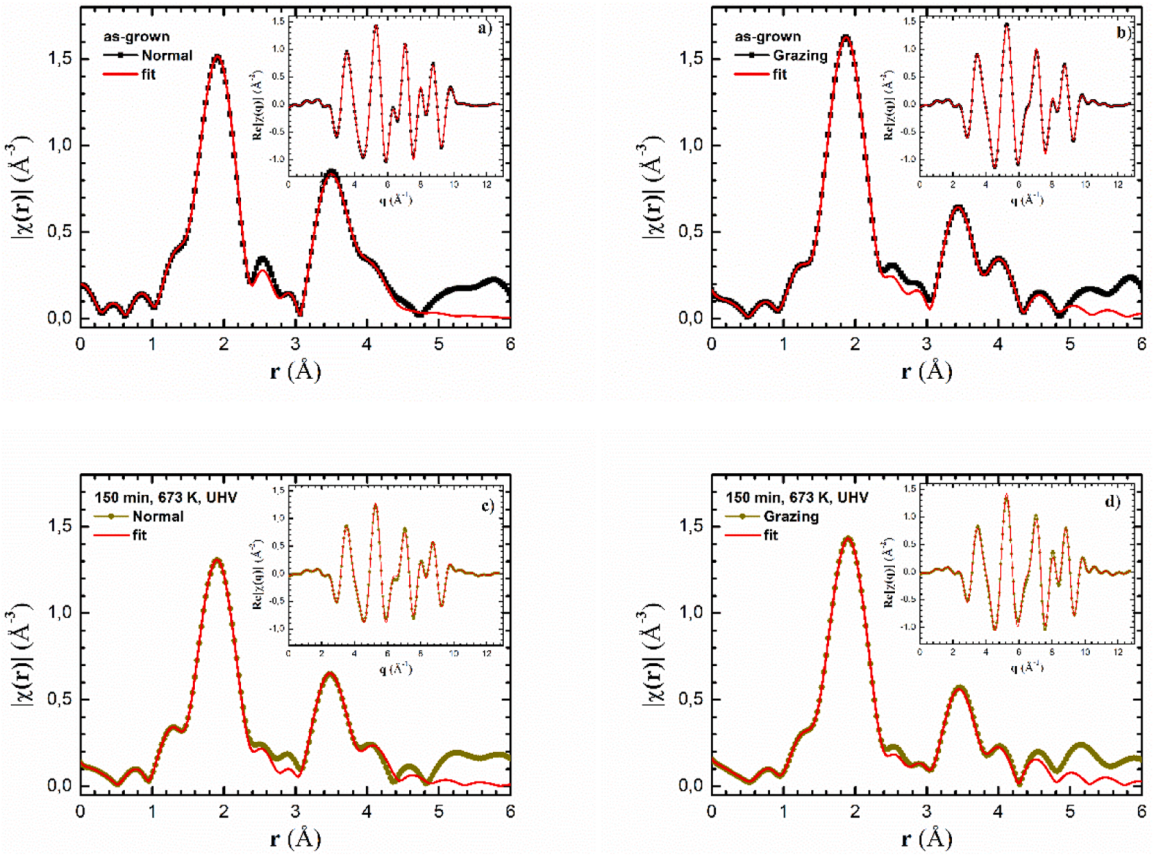

Fig. 2. Comparison between the experimental spectra and the best fit of modulus of Fourier Transform of $k^2\chi(k)$ EXAFS spectra for the as-grown sample (a and b) and the 150 minutes annealing at 673 K under UHV (c and d) in both polarization geometries. In the inset of each figure the real part of the back Fourier Transform χ(q) is presented to show the quality of the fitting.

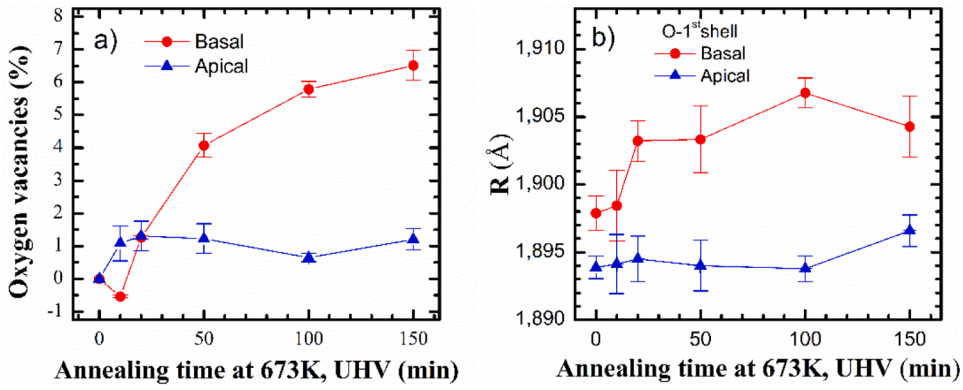

Fig. 3. (a) Percentage of vacancies for the basal and apical oxygens as a function of the annealing time. (b) Evolution of the first neighbors distance in respect to the Mn absorbing atom as a function of the annealing time.

together with an increase of the bond length, while at the octahedral apices the oxygen effective coordination number and bond lengths remain constant. This effect suggests that the generated oxygen vacancies are mainly located at the octahedral basal plane. Up to 6.5% of oxygen vacancies have been determined at the basal plane for 150 minutes annealing time compared to 2% at the apical position. The transport properties have been correlated with the lattice oxygen defects, indicating a linear dependency of the MIT temperature with the amount of oxygen defects, in agreement with previous works.

CRediT authorship contribution statement

E. Salas-Colera: Writing – Original draft, Writing - review & editing, Formal analysis, Investigation. **A. Muñoz-Noval**: Investigation, Writing - review & editing. **E. Sebastiani-Tofano**: Investigation, Writing - review & editing. **G.R. Castro**: Conceptualization, Funding acquisition. **J. Rubio-Zuazo**: Conceptualization, Writing - review & editing, Supervision.

Declaration of Competing Interest

The authors declare that they have no known competing financial

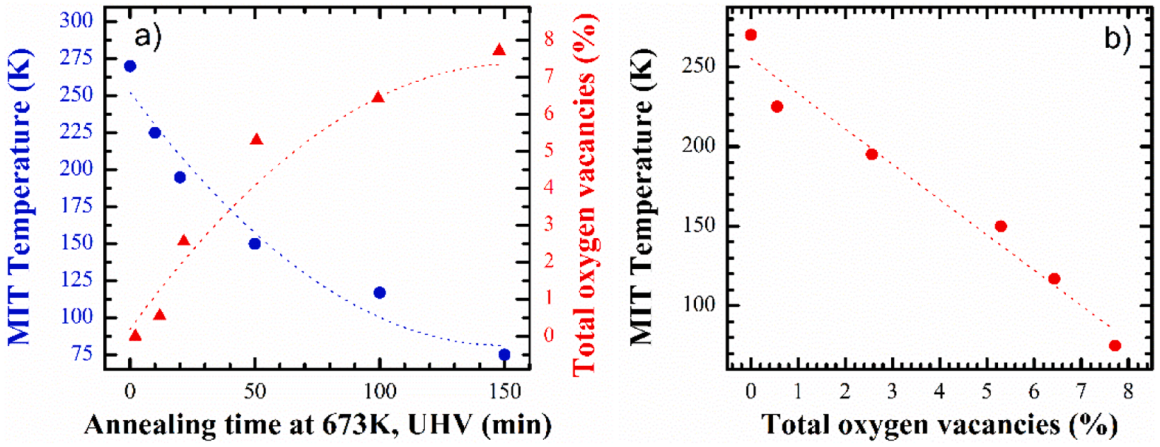

Fig. 4. (a) Evolution of the MIT temperature and calculated total percentage of oxygen vacancies as a function of the annealing time. (b) MIT temperature behavior as a function of the total amount of oxygen vacancies.

interests or personal relationships that could have appeared to influence the work reported in this paper.

Data availability

Data will be made available on request.

Acknowledgments

The authors are grateful to the BM25-SpLine Staff for their valuable help and for the financial support from the Spanish MCIN and Consejo Superior de Investigaciones Científicas [Grant Nos. 2010-6-OE-013 and 2021-6-OE-030]. E.S.C. acknowledge financial support of Comunidad de Madrid (Spain) - multiannual agreement with UC3M ("Fostering Young Doctors Research", NANOSOLREC), and in the context of the V PRICIT (Research and Technological Innovation Regional Programme).

References

[1] E. Dagotto, T. Hotta, A. Moreo, Colossal magnetoresistant materials: the key role of phase separation, Phys. Rep. 344 (2001) 1–153, https://doi.org/10.1016/S0370-1573(00)00121-6.
[2] A. de Andrés, J. Rubio, G. Castro, S. Taboada, J.L. Martínez, J.M. Colino, Structural and magnetic properties of ultrathin epitaxial La0.7Ca0.3MnO3 manganite films: strain versus finite size effects, Appl. Phys. Lett. 83 (2003) 713, https://doi.org/10.1063/1.1594838.
[3] P.R. Sagdeo, S. Anwar, N.P. Lalla, Powder X-ray diffraction and rietveld analysis of La1−xCaxMnO3 (0< X <1), Powder Diffr. 21 (2006) 40–44, https://doi.org/10.1154/1.2104536.
[4] J. Fontcuberta, B. Martínez, A. Seffar, S. Piñol, J.L. García-Muñoz, X. Obradors, Colossal magnetoresistance of ferromagnetic manganites: structural tuning and mechanisms, Phys. Rev. Lett. 76 (1996) 1122–1125, https://doi.org/10.1103/PhysRevLett.76.1122.
[5] C.H. Booth, F. Bridges, G.H. Kwei, J.M. Lawrence, A.L. Cornelius, J.J. Neumeier, Lattice Effects in La1-xCaxMnO3 (x:0 to 1): Relationships between Distortions, Charge Distribution, and Magnetism (1998).
[6] E. Dagotto, Open questions in CMR manganites, relevance of clustered states and analogies with other compounds including the cuprates, New J. Phys. 7 (2005), https://doi.org/10.1088/1367-2630/7/1/067.
[7] Y. Lu, X.W. Li, G.Q. Gong, G. Xiao, A. Gupta, Large magnetotunneling effect at low magnetic fields in micrometer-scale epitaxial La0.67Sr0.33MnO3 tunnel junctions, Phys. Rev. B 54 (1996) R8357–R8360, https://doi.org/10.1103/PhysRevB.54.R8357.
[8] S. Mercone, C.A. Perroni, V. Cataudella, C. Adamo, M. Angeloni, C. Aruta, G. De Filippis, F. Miletto, A. Oropallo, P. Perna, A.Y. Petrov, U. Scotti Di Uccio, L. Maritato, Transport properties in manganite thin films, Phys. Rev. B Condens. Matter Mater. Phys. 71 (2005) 064415, https://doi.org/10.1103/PhysRevB.71.064415.
[9] S. Jin, M. McCormack, T.H. Tiefel, R. Ramesh, Colossal magnetoresistance in La-Ca-Mn-O ferromagnetic thin films (invited), J. Appl. Phys. 76 (1994) 6929–6933, https://doi.org/10.1063/1.358119.
[10] S. Jin, T.H. Tiefel, M. McCormack, L.H. Chen, R. Ramesh, D. Schurig, Thickness dependence of magnetoresistance in La-Ca-Mn-O epitaxial films, Appl. Phys. Lett. 67 (1995) 557–559, https://doi.org/10.1063/1.115168.
[11] M. McCormack, S. Jin, T.H. Tiefel, R.M. Fleming, J.M. Phillips, R. Ramesh, Very large magnetoresistance in perovskite-like La-Ca-Mn-O thin films, Appl. Phys. Lett. 64 (1994) 3045–3047, https://doi.org/10.1063/1.111372.
[12] J. Rubio-Zuazo, L. Onandia, P. Ferrer, G.R. Castro, Correlation between the electronic and atomic structure, transport properties, and oxygen vacancies on La0.7Ca0.3MnO3 thin films, Appl. Phys. Lett. 104 (2014) 21604, https://doi.org/10.1063/1.4861385.
[13] H. Guo, J.O. Wang, X. He, Z. Yang, Q. Zhang, K.J. Jin, C. Ge, R. Zhao, L. Gu, Y. Feng, W. Zhou, X. Li, Q. Wan, M. He, C. Hong, Z. Guo, C. Wang, H. Lu, K. Ibrahim, S. Meng, H. Yang, G. Yang, The origin of oxygen vacancies controlling La2/3Sr1/3MnO3 electronic and magnetic properties, Adv. Mater. Interfaces 3 (2016) 1500753, https://doi.org/10.1002/admi.201500753.
[14] C. Ge, K.J. Jin, L. Gu, L.C. Peng, Y.S. Hu, H.Z. Guo, H.F. Shi, J.K. Li, J.O. Wang, X. X. Guo, C. Wang, M. He, H.Bin Lu, G.Z. Yang, Metal-insulator transition induced by oxygen vacancies from electrochemical reaction in ionic liquid-gated manganite films, Adv. Mater. Interfaces 2 (2015) 1500407, https://doi.org/10.1002/admi.201500407.
[15] J.M. Börgers, R.A. De Souza, The surprisingly high activation barrier for oxygen-vacancy migration in oxygen-excess manganite perovskites, Phys. Chem. Chem. Phys. 22 (2020) 14329–14339, https://doi.org/10.1039/d0cp01281e.
[16] M. Pavone, A.B. Muñoz-García, A.M. Ritzmann, E.A. Carter, First-principles study of lanthanum strontium manganite: insights into electronic structure and oxygen vacancy formation, J. Phys. Chem. C 118 (2014) 13346–13356, https://doi.org/10.1021/jp500352h.
[17] H.A. Tahini, X. Tan, U. Schwingenschlögl, S.C. Smith, Formation and migration of oxygen vacancies in SrCoO3 and their effect on oxygen evolution reactions, ACS Catal. 6 (2016) 5565–5570, https://doi.org/10.1021/acscatal.6b00937.
[18] M.T. Curnan, J.R. Kitchin, Effects of concentration, crystal structure, magnetism, and electronic structure method on first-principles oxygen vacancy formation energy trends in perovskites, J. Phys. Chem. C 118 (2014) 28776–28790, https://doi.org/10.1021/jp507957n.
[19] H.Y. Su, K. Sun, DFT study of the stability of oxygen vacancy in cubic ABO3 perovskites, J. Mater. Sci. 50 (2015) 1701–1709, https://doi.org/10.1007/s10853-014-8731-0.
[20] I. Tanaka, F. Oba, K. Tatsumi, M. Kunisu, M. Nakano, H. Adachi, Theoretical formation energy of oxygen-vacancies in oxides, Mater. Trans. 43 (2002), 1426–1426.
[21] G.R. Castro, Optical design of the general-purpose Spanish X-ray beamline for absorption and diffraction, J. Synchrotron Radiat. 5 (1998) 657–660, https://doi.org/10.1107/S090904959701907.
[22] B. Ravel, M. Newville, ATHENA, ARTEMIS, HEPHAESTUS: data analysis for X-ray absorption spectroscopy using IFEFFIT, J. Synchrotron Radiat. 12 (2005) 537–541, https://doi.org/10.1107/S0909049505012719.
[23] A. Manceau, W.P. Gates, D. Chateigner, Polarized EXAFS, distance-valence least-squares modeling (DVLS), and quantitative texture analysis approaches to the structural refinement of Garfield nontronite, Phys. Chem. Miner. 25 (1998) 347–365, https://doi.org/10.1007/s002690050125.
[24] D.D. Khalyavin, P. Manuel, W. Yi, A.A. Belik, Spin and orbital ordering in TlMnO3: neutron diffraction study, Phys. Rev. B 94 (2016) 134412, https://doi.org/10.1103/PhysRevB.94.134412.
[25] J. Rodríguez-Carvajal, M. Hennion, F. Moussa, A.H. Moudden, L. Pinsard, A. Revcolevschi, Neutron-diffraction study of the Jahn-Teller transition in stoichiometric LaMnO3, Phys. Rev. B 57 (1998) R3189–R3192, https://doi.org/10.1103/PhysRevB.57.R3189.

[26] S.D. Kelly, B. Ravel, EXAFS energy shift and structural parameters, AIP Conf. Proc. 882 (2007) 132–134, https://doi.org/10.1063/1.2644451.
[27] J.J. Rehr, E.A. Stern, R.L. Mertint, E.R. Davidson, Extended x-ray-absorption fine-structure amplitudes-Wave-function relaxation and chemical effects, Phys. Rev. B 17 (1978) 560–565, https://doi.org/10.1103/PhysRevB.17.560.
[28] D.C. Koningsberger, R. Prins. X-Ray Absorption: Principles, Applications, Techniques of EXAFS, SEXAFS and XANES, Wiley, New York, 1987.